



Are hierarchically formed embedded star clusters surviving gas expulsion depending on their initial conditions?

Downloaded from: <https://research.chalmers.se>, 2024-04-20 06:18 UTC

Citation for the original published paper (version of record):

Dominguez, R., Farias Osses, J., Fellhauer, M. et al (2021). Are hierarchically formed embedded star clusters surviving gas expulsion depending on their initial conditions?. *Monthly Notices of the Royal Astronomical Society*, 508(4): 5410-5424.
<http://dx.doi.org/10.1093/mnras/stab2644>

N.B. When citing this work, cite the original published paper.

Are hierarchically formed embedded star clusters surviving gas expulsion depending on their initial conditions?

R. Domínguez,^{1★} J. P. Farias,² M. Fellhauer^{id}³ and Ralf S. Klessen^{id}^{1,4}

¹*Institut für Theoretische Astrophysik, Zentrum für Astronomie, Universität Heidelberg, Albert-Ueberle-Straße 2, D-69120 Heidelberg, Germany*

²*Department of Space, Earth & Environment, Chalmers University of Technology, SE-412 96 Gothenburg, Sweden*

³*Departamento de Astronomía, Universidad de Concepción, Casilla 160-C, Concepción, Chile*

⁴*Interdisziplinäres Zentrum für Wissenschaftliches Rechnen, Universität Heidelberg, Im Neuenheimer Feld 205, D-69120 Heidelberg, Germany*

Accepted 2021 September 9. Received 2021 September 7; in original form 2021 March 18

ABSTRACT

We investigate the dissolution process of young embedded star clusters with different primordial mass segregation levels using fractal distributions by means of N -body simulations. We combine several star clusters in virial and subvirial global states with Plummer and uniform density profiles to mimic the gas. The star clusters have masses of $M_{\text{stars}} = 500 M_{\odot}$ that follow an initial mass function where the stars have maximum distance from the centre of $r = 1.5$ pc. The clusters are placed in clouds that at the same radius have masses of $M_{\text{cloud}} = 2000 M_{\odot}$, resulting in star formation efficiency of 0.2. We remove the background potential instantaneously at a very early phase, mimicking the most destructive scenario of gas expulsion. The evolution of the fraction of bound stellar mass is followed for a total of 16 Myr for simulations with stellar evolution and without. We compare our results with previous works using equal-mass particles where an analytical physical model was used to estimate the bound mass fraction after gas expulsion. We find that independent of the initial condition, the fraction of bound stellar mass can be well predicted just right after the gas expulsion but tends to be lower at later stages, as these systems evolve due to the stronger two-body interactions resulting from the inclusion of a realistic initial mass function. This discrepancy is independent of the primordial mass segregation level.

Key words: methods: numerical – galaxies: star formation – galaxies: star clusters: general.

1 INTRODUCTION

Young star clusters are usually found embedded in molecular clouds from which they were recently born. Their early evolution is dominated by feedback processes such as ultraviolet radiation and massive stellar winds from OB stars, or supernova (SN) explosions, that eventually remove the natal gas. As gas is expelled, star clusters lose gravitational potential resulting in their dissolution into the field (see e.g. Tutukov 1978; Hills 1980; Margulis, Lada & Dearborn 1984; Goodwin 1997; Adams 2000; Geyer & Burkert 2001; Boily & Kroupa 2003a, b; Fellhauer & Kroupa 2005; Bastian & Goodwin 2006; Baumgardt & Kroupa 2007; Smith et al. 2011; Lee & Goodwin 2016; Brinkmann et al. 2017; Farias, Tan & Chatterjee 2017; Shukirgaliyev et al. 2017, 2018, 2020; Farias et al. 2018). In most scenarios, the feedback is assumed to be strong enough to disrupt the molecular cloud completely, preventing any further star formation (Wang et al. 2010; Murray 2011).

Seminal studies like that of Baumgardt & Kroupa (2007) have shown that if gas expulsion happens instantly, e.g. by an SNe explosion, only star clusters with global star formation efficiency (SFE) higher than 0.2 can retain a fraction of bound stars after the gas is gone. This SFE limit can decrease if gas expulsion happens over larger time-scales since stars have time to adjust to the change in the gravitational potential. However, later studies

have indicated that other aspects can also bring down this limit, for instance, if the gas is distributed in a less concentrated form, its contribution to the binding potential of the cluster becomes less important (Shukirgaliyev et al. 2017). Additionally, a wide range of post-gas-expulsion bound fractions can be found if star clusters are formed hierarchically, since the relaxation processes that erase substructure can also raise the effective SFE within the half-mass radius of star clusters by the time gas expulsion happens (Smith et al. 2011). There are other aspects that have also been ignored so far. For instance, most of the previous studies are based on equal-mass particles to exclude the effects of strong dynamical interactions between different mass stars, to isolate the effect of the different processes under study. However, stars have a wide range of masses, and an important aspect that is currently under active debate is whether massive stars are born in preferential locations within the star-forming regions (Zinnecker 1982; Murray & Lin 1996; Bonnell et al. 2001; Elmegreen & Krakowski 2001; Klessen 2001; Bonnell & Bate 2006; Girichidis et al. 2012), for instance, in the densest gas-rich areas where they can continuously accrete material competing with neighbour stars for this material, a scenario referred as competitive accretion (Larson 1982; Murray & Lin 1996; Bonnell et al. 1997). Evidence of this scenario has been detected in embedded star clusters (see e.g. Lada, Alves & Lada 1996; Hillenbrand 1997; Hillenbrand & Hartmann 1998; Bonatto & Bica 2006; Chen, de Grijs & Zhao 2007; Er, Jiang & Fu 2013; Dib & Henning 2019). Mass segregation has also been shown to develop dynamically (McMillan, Vesperini & Portegies Zwart 2007; Allison et al. 2009a; Yu, de Grijs & Chen 2011)

* E-mail: raul.dominguez@stud.uni-heidelberg.de

and on short time-scales (Allison et al. 2010; Parker et al. 2016), e.g. within ~ 1 Myr. In some systems, dynamical processes are not fast enough to explain the high level of mass segregation observed, therefore some degree of mass primordial segregation is needed to explain such high concentration of massive stars (Bonnell & Davies 1998; Raboud & Mermilliod 1998).

On the other hand, Parker & Goodwin (2015) point out that stars formed by competitive accretion rarely result in a segregated cluster. Motivated by the large theoretical and observational evidence that star clusters are formed in hierarchical distributions (Whitmore et al. 1999; Johnstone et al. 2000; Kirk, Johnstone & Tafalla 2007; Schmeja, Kumar & Ferreira 2008; Gutermuth et al. 2009; di Francesco et al. 2010; Könyves et al. 2010; Maury et al. 2011; Wright et al. 2014), Domínguez et al. (2017) found a level of mass segregation in the early stages of the embedded phase even starting with non-segregated substructured clusters, and also that a very high artificial level of mass segregation is not stable and it is quickly decreased by dynamical processes followed by a lower segregated state (see also e.g. Allison et al. 2009b, 2010). If different levels of mass segregation affect the posterior evolution of clusters after gas expulsion are still an open question.

Note though as a caveat to the hypothesis that star clusters form hierarchically from the mergers of smaller clusters: the projection of filamentary star formation within a part of a single molecular cloud, with well-separated and not merging embedded clusters spread along filaments, may appear, from the distant observer’s point of view, as a sub-clustered cluster. Banerjee & Kroupa (2018) showed that the compactness and ages of observed very young clusters, such as the Orion Nebula Cluster, NGC 3603 and R136, significantly constrain the hierarchical merging scenario.

Farias et al. (2015, 2018) proposed two predictions to estimate the bound mass fraction remaining after violent gas expulsion for models that were representing embedded star clusters using as a first approach, equal-mass particles in order to study one parameter at time. Here, as a next step, we include the effects of particles having different masses following a typical initial stellar mass function (IMF) that add stronger two-body different mass interactions and mass segregation. The same sample is studied with stellar evolution (SEV) using winds and SNe. We test if the predictions proposed by Farias et al. (2015, 2018) are still valid using this expanded framework.

The structure of the paper is as follows. In Section 2, we describe our method and the initial conditions. In Section 3, we explain our sample of simulations and in Section 4 we show our results. We end in Section 5 with our summary and conclusion.

2 METHOD AND INITIAL CONDITIONS

2.1 Fractal distributions and initial mass function

As in our previous work, we follow the set-up described in Farias et al. (2015, 2018) and Domínguez et al. (2017). Following the method described in Goodwin & Whitworth (2004), we generate initially substructured distributions with a fractal dimension of $D = 1.6$, with a maximum radius of 1.5 pc, and a total stellar mass of $500 M_{\odot}$.

We assign individual stellar masses using the modified¹ initial mass function of Kroupa (2002) given by

$$N(M) \propto \begin{cases} M^{-1.30} & m_0 \leq M/M_{\odot} < m_1 \\ M^{-2.30} & m_1 \leq M/M_{\odot} < m_2 \\ M^{-2.35} & m_2 \leq M/M_{\odot} < m_3 \end{cases}, \quad (1)$$

¹We avoid the substellar mass range below $0.08 M_{\odot}$ for brown dwarfs.

with $m_0 = 0.08$, $m_1 = 0.5$, $m_2 = 1.0$, and $m_3 = 50 M_{\odot}$. Using this initial mass function, we obtain a total number of stars of ~ 1000 , and a average stellar mass of $0.5 M_{\odot}$.

2.2 Mass segregation using the Λ_{MSR} parameter

The focus of this study is to examine if primordial levels of mass segregation influence the later evolution of star clusters. We define all stars with $M \geq 4 M_{\odot}$ as massive stars while the rest are considered low-mass stars. We quantify the different levels of mass segregation using the ‘mass segregation ratio’ parameter (Λ_{MSR}) introduced by Allison et al. (2009a). Λ_{MSR} is calculated by first finding the length of the shortest path joining the N_{MST} most massive stars, i.e. the minimum spanning tree (MST) length, l_{massive} . Secondly, the average MST length of N_{massive} random stars $\langle l_{\text{norm}} \rangle$ is calculated with its associated standard deviation σ_{norm} . Finally, Λ_{MSR} is defined as

$$\Lambda_{\text{MSR}} = \frac{\langle l_{\text{norm}} \rangle}{l_{\text{massive}}} \pm \frac{\sigma_{\text{norm}}}{l_{\text{massive}}}, \quad (2)$$

where a value of $\Lambda_{\text{MSR}} \sim 1$ indicates no mass segregation, i.e. low- and high-mass stars are uniformly distributed. $\Lambda_{\text{MSR}} \gg 1$ indicates strong mass segregation, i.e. massive stars are located close to each other. $\Lambda_{\text{MSR}} < 1$ means inverse mass segregation, i.e. high-mass stars are more dispersed than low-mass stars. In this work, we explore different levels of mass segregation. These are achieved by locating the massive stars:

- (i) randomly in a radius $r > 0.5$ pc until finding $\Lambda_{\text{MSR}} \sim 1$, i.e. a cluster without mass segregation which hereafter is referred as NOSEG.
- (ii) We force all massive stars to be located in a radius $r < 0.5$ pc until obtaining $4 < \Lambda_{\text{MSR}} < 5$, i.e. primordial mass segregated clusters, hereafter referred as SEG.

An example of two fractal distributions with different levels of mass segregation is shown in Fig. 1. The top panel shows a strongly mass segregated (SEG) fractal star cluster, for this case we have $\Lambda_{\text{MSR}} = 5.2 \pm 1.1$. The bottom panel shows a non-segregated (NOSEG) fractal star cluster with $\Lambda_{\text{MSR}} = 1.0 \pm 0.2$ where massive stars are spread along the distribution. In both panels, blue plus symbols (+) represent low-mass stars ($M < 4 M_{\odot}$) and red circles represent massive stars ($M > 4 M_{\odot}$). The sizes of the symbols are proportional to the mass of the stars but for massive stars the sizes have been multiplied by 15 for better appreciation.

2.3 Background potential

We use two different descriptions for the distribution of the background gas (BG). One, assuming the gas is centrally concentrated, represented by a Plummer (1911) sphere, with a density radial profile, $\rho(r)$, described by

$$\rho(r) = \frac{3M_{\text{Pl}}}{4\pi R_{\text{Pl}}^3} \left(1 + \frac{r^2}{R_{\text{Pl}}^2} \right)^{-\frac{5}{2}} \quad (3)$$

with M_{Pl} and R_{Pl} the Plummer Mass and Plummer radius, respectively, and r being the distance to the centre of the cloud. The enclosed mass $M(r)$ within Plummer sphere is

$$M(r) = M_{\text{Pl}} \frac{r^3}{R_{\text{Pl}}^3} \left(1 + \frac{r^2}{R_{\text{Pl}}^2} \right)^{-\frac{3}{2}}, \quad (4)$$

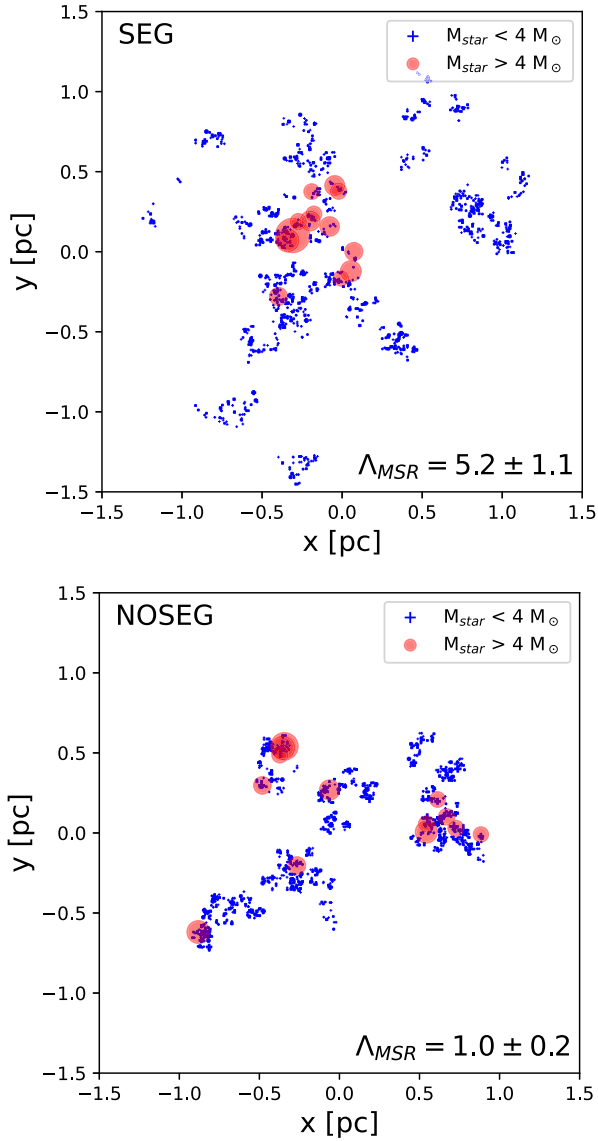


Figure 1. Two different fractal distributions. The top panel shows a cluster with mass segregation (SEG) and bottom panel a cluster non-segregated (NOSEG). Low-mass stars ($M < 4 M_{\odot}$) are represented with blue plus symbols (+) and massive stars ($M \geq 4 M_{\odot}$) with red circles. The sizes of the points are associated with the mass of the stars. The size of the massive stars is multiplied by five times for a better appreciation of their location.

which produces a BG potential $\phi(r)$ as follows:

$$\phi(r) = -\frac{GM_{\text{pl}}}{R_{\text{pl}}} \left(1 + \frac{r^2}{R_{\text{pl}}^2}\right)^{-\frac{1}{2}}, \quad (5)$$

where G is the gravitational constant.

The second set of models assumes the BG is uniformly distributed within the cloud. In this case, the density profile is constant with a value:

$$\rho(r) = \frac{3M_{\text{tot}}}{4\pi r_c^3}, \quad r < r_c \quad (6)$$

where M_{tot} is the total mass of the sphere and r_c is the radius of the sphere truncated to be 1.8 pc. The enclosed $M(r)$ within a uniform

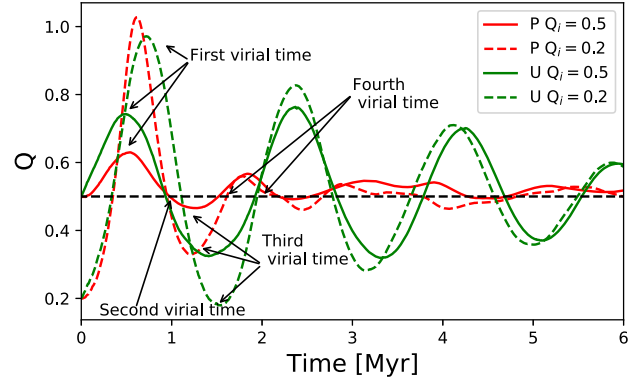


Figure 2. Example of Q evolution in time with different initial virial states under different BG distributions. Red line shows the evolution of Q for a model under a Plummer (P) BG profile and green line for a model with a uniform (U) distribution. Solid and dashed lines show models with virial ($Q_i = 0.5$) and subvirial ($Q_i = 0.2$) initial velocities. First, second, third, and fourth virial times are pointed with arrows and they are the moments when the BG is removed. Dashed black line shows the virial equilibrium value of $Q = 0.5$.

sphere is described by

$$M(r) = \frac{M_{\text{tot}}}{r_c^3} r^3, \quad r < r_c \quad (7)$$

and its respective BG potential $\phi(r)$ inside and outside of the sphere as follows:

$$\phi(r) = \frac{GM_{\text{tot}}}{2r_c^3} (r^2 - 3r_c^2), \quad r < r_c, \quad (8)$$

$$\phi(r) = \frac{GM_{\text{tot}}}{r}, \quad r > r_c. \quad (9)$$

The total mass for the background sphere of gas is chosen ensuring a global SFE = 0.2 within a radius of 1.5 pc where the total mass in stars is $\sim 500 M_{\odot}$. For the case of the Plummer sphere this is achieved by setting $M_{\text{pl}} = 3472 M_{\odot}$ and $R_{\text{pl}} = 1.0$ pc. For the uniform sphere case, $M_{\text{tot}} = 3455 M_{\odot}$. We use these values in order to have a direct comparison with Farias et al. (2015, 2018) and Domínguez et al. (2017), which are justified following a similar set-up as in the classical picture of Baumgardt & Kroupa (2007) and observations (see e.g. Megeath et al. 2016).

2.4 Initial virial state

The virial ratio is defined as

$$Q = \frac{T}{|\Omega|}, \quad (10)$$

where T and Ω are the total kinetic and potential energy of the system, respectively.²

In this work, we investigate two different initial dynamical states of star clusters, a subvirial state represented by $Q = 0.2$ and virial equilibrium state with $Q = 0.5$. We note, however, that the latter does not represent a system in equilibrium, rather a system with velocities that match virial equilibrium. The fractal distributions used here are far from an equilibrium system therefore these systems will pursue an equilibrium distribution. The rearrangement of stars and energy

²In latest literature Q value is also found referred to α but we keep the symbol to be consistent with our line of papers.

Table 1. Summary of initial conditions used for our study. The first column shows the initial stellar distribution, the second column shows the value of the initial virial ratio, the third and fourth columns indicate the number of different fractal distributions and IMF samples, respectively. BG profile is provided in the fifth column. The sixth column indicates the different virial times when the gas is expelled, and the seventh column shows the number of realizations for each set. The eighth column shows cases where stellar evolution is included.

Initial mass distribution	Initial virial ratio	Fractals	IMF	BG potential	Virial time	Number of simulations	Stellar evolution
SEG	0.5	10	10	Plummer/Uniform	1/2/3/4	100/100/100/100	No
SEG	0.2	10	10	Plummer/Uniform	1/2/3/4	100/100/100/100	No
SEG	0.5	10	10	Plummer/Uniform	1/2/3/4	100/100/100/100	Yes
SEG	0.2	10	10	Plummer/Uniform	1/2/3/4	100/100/100/100	Yes
NOSEG	0.5	10	10	Plummer/Uniform	1/2/3/4	100/100/100/100	No
NOSEG	0.2	10	10	Plummer/Uniform	1/2/3/4	100/100/100/100	No
NOSEG	0.5	10	10	Plummer/Uniform	1/2/3/4	100/100/100/100	Yes
NOSEG	0.2	10	10	Plummer/Uniform	1/2/3/4	100/100/100/100	Yes
EQUAL	0.5	100	0	Plummer/Uniform	1/2/3/4	100/100/100/100	No
EQUAL	0.2	100	0	Plummer/Uniform	1/2/3/4	100/100/100/100	No

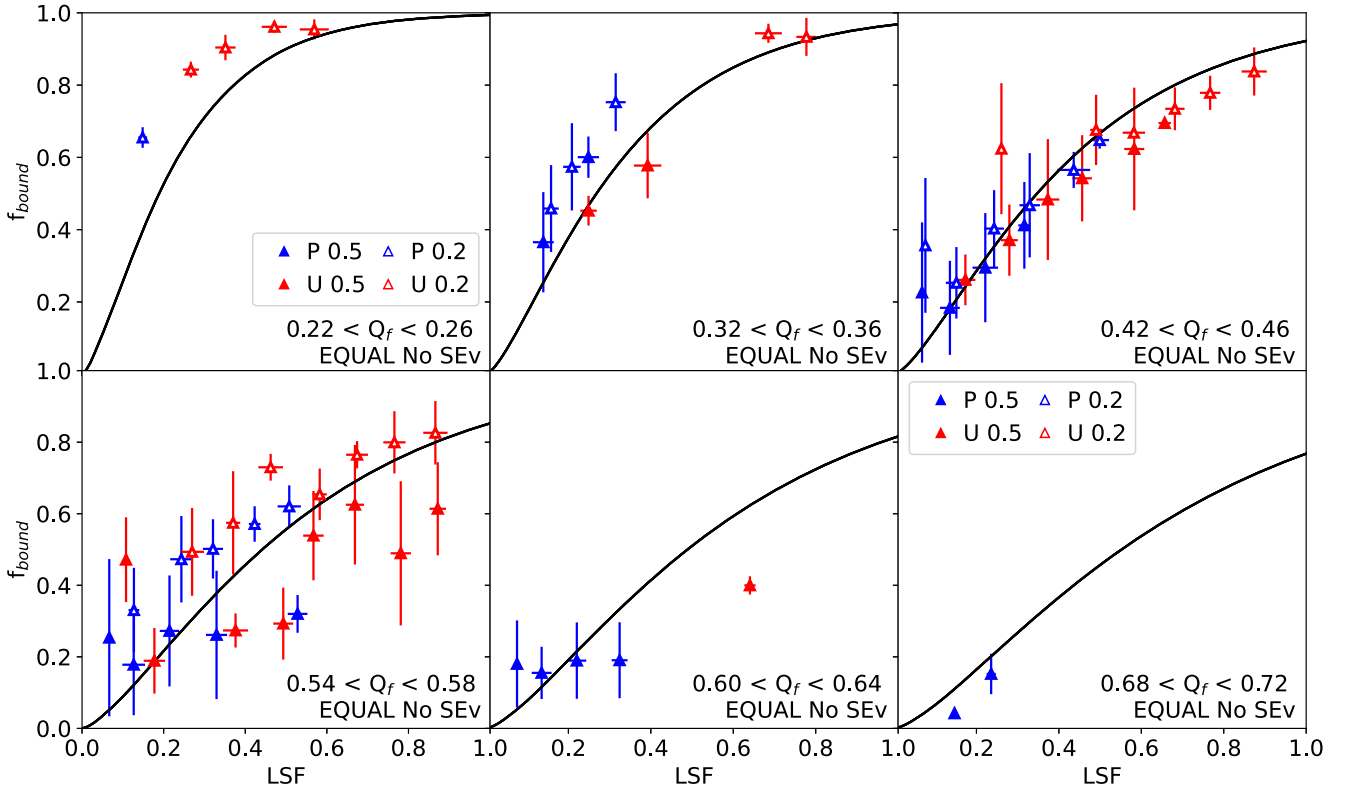


Figure 3. f_{bound} versus LSF for equal-mass particle simulations without stellar evolution at 16 Myr for VT = 1 (bottom row) and VT = 3 (top row). Blue and red triangles are simulations with Plummer (P) and Uniform (U) BG potential, respectively. The initial virial ratios $Q_i = 0.5$ and $Q_i = 0.2$ are represented by filled and empty symbols, respectively. The solid black line shows the predictive model introduced by Farias et al. (2015), i.e. equation (12), using the central value of Q_f in each respective panel.

causes the measured virial ratio to oscillate around an equilibrium value as the clusters evolve. An example of the evolution of Q with time under different conditions can be seen in Fig. 2 where the red line shows the evolution of one fractal cluster in a Plummer BG and the green line for the same fractal cluster but now under the influence of a uniform BG distribution. Solid and dashed lines represent the initial states $Q_i = 0.5$ and $Q_i = 0.2$, respectively. The horizontal dashed black line represents the virial state $Q = 0.5$. As expected subvirial star clusters show a larger amplitude of the oscillation of Q with time relative to the $Q_i = 0.5$ case. Stars in a cluster with

$Q_i = 0.2$ tend to have orbits that fall through the centre of potential of the system, reaching high velocities as they cross the potential minimum. While stars in systems with $Q_i = 0.5$ tend to have more circular and stable orbits.

2.5 Virial evolution and gas expulsion

In Fig. 2, we point out different locations of the evolution of Q . At the selected points, we emulate rapid gas expulsion by removing the influence of the BG. Different locations on the oscillation of the

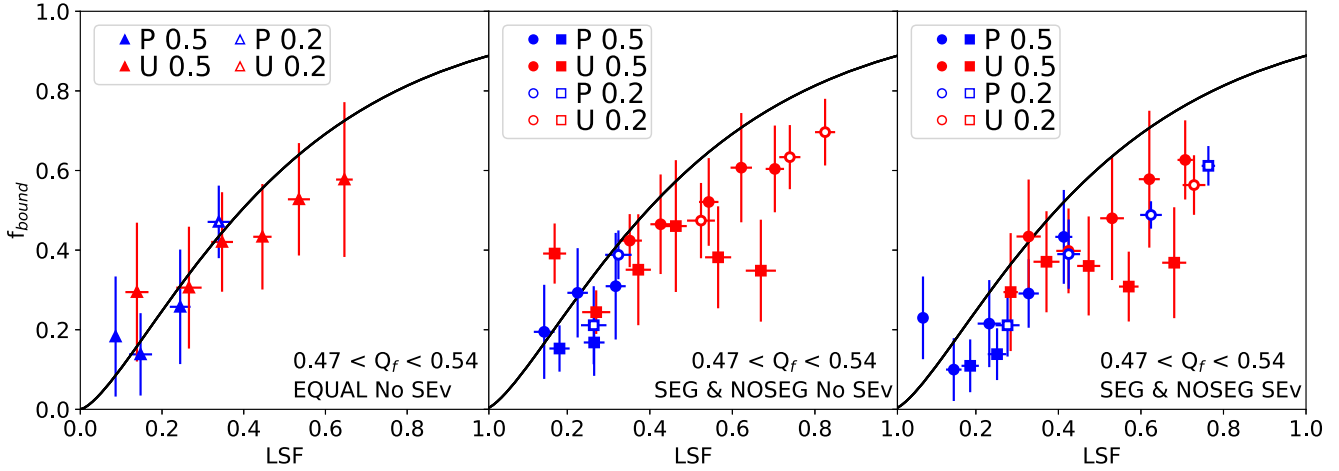


Figure 4. f_{bound} versus LSF only for $Q_f = 0.5$ (only reached when $VT = 2$ and $VT = 4$). The left-hand panel is for equal-mass simulations and it uses the same colours and symbols as in Fig. 3 where the black line is equation (12). The central panel shows results for simulations using IMF and non-stellar evolution. SEG simulations are shown with circles and NOSEG simulations are shown with squares. The right-hand panel is similar as the central one but now for simulations using stellar evolution.

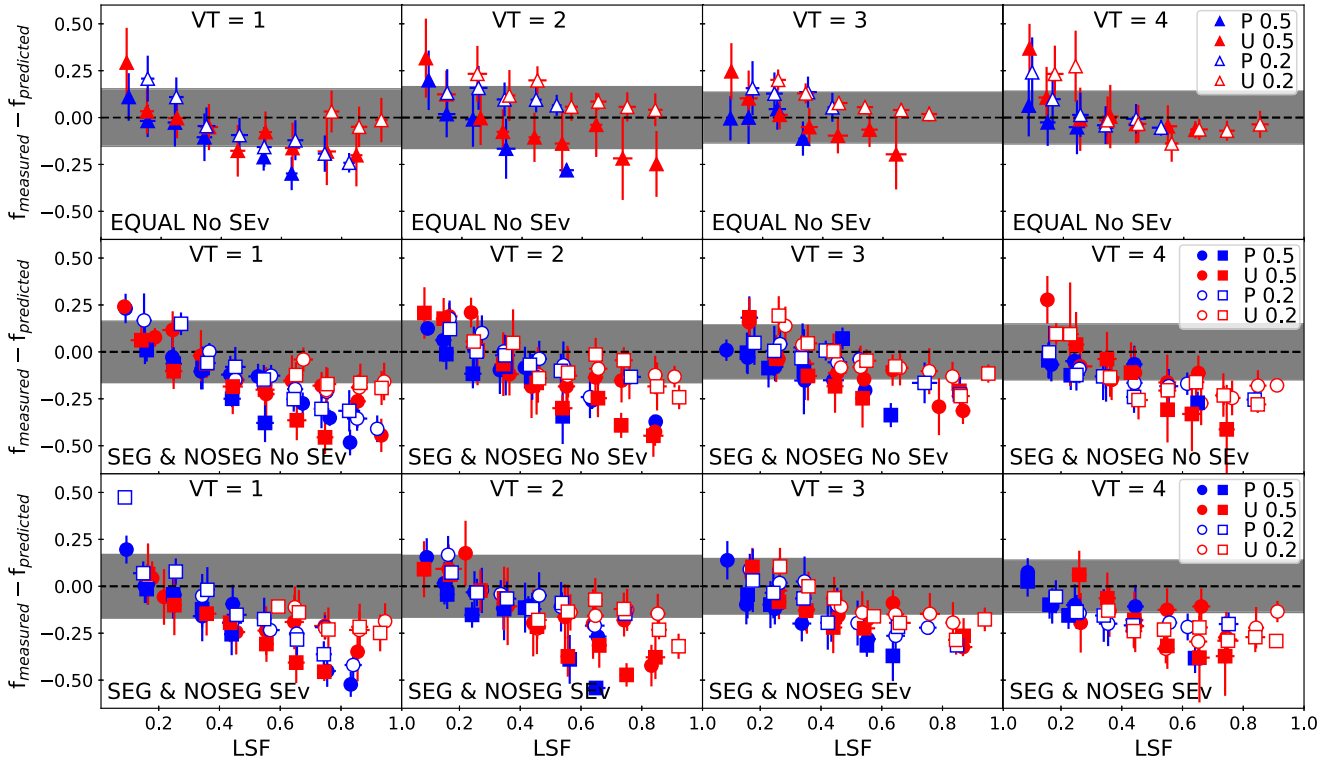


Figure 5. Average difference between the measured bound fraction (f_{measured}) and the predicted bound fraction ($f_{\text{predicted}}$) from equation (12) versus LSF. The black dashed line represents a zero difference with the prediction. The panels are ordered from left to right by virial time (VT) and from top to bottom as in Fig. 4 (now vertically) with the respective colour and symbols. The grey area represents the average 1σ error for all the result in each panel.

virial ratio are referred as virial time (VT). We call the first peak in the evolution of Q ‘First virial time’. At this point, star clusters are supervirial and we can obtain star clusters with pre-gas expulsion virial ratio of $Q_f > 0.5$. The exact values of Q_f vary between the different models. After this first maximum, the cluster passes through a state with $Q = 0.5$, we term this point ‘Second virial time’. All star clusters at this point have the same value of Q_f . Then, star clusters reach a first minimum of Q , the ‘Third virial time’. Here, star clusters

have subvirial velocities and therefore we can obtain star clusters with $Q_f < 0.5$ within a range of values. Finally, star clusters reach $Q = 0.5$ again, after the first minimum, we call this point ‘Fourth virial time’. By simplicity, we refer to them as VT = 1, 2, 3, 4, respectively. Note that these four points in the evolution of star clusters are different for each individual cluster. Therefore, for each set of initial conditions, we run four simulations removing the BG potential at these four different times.

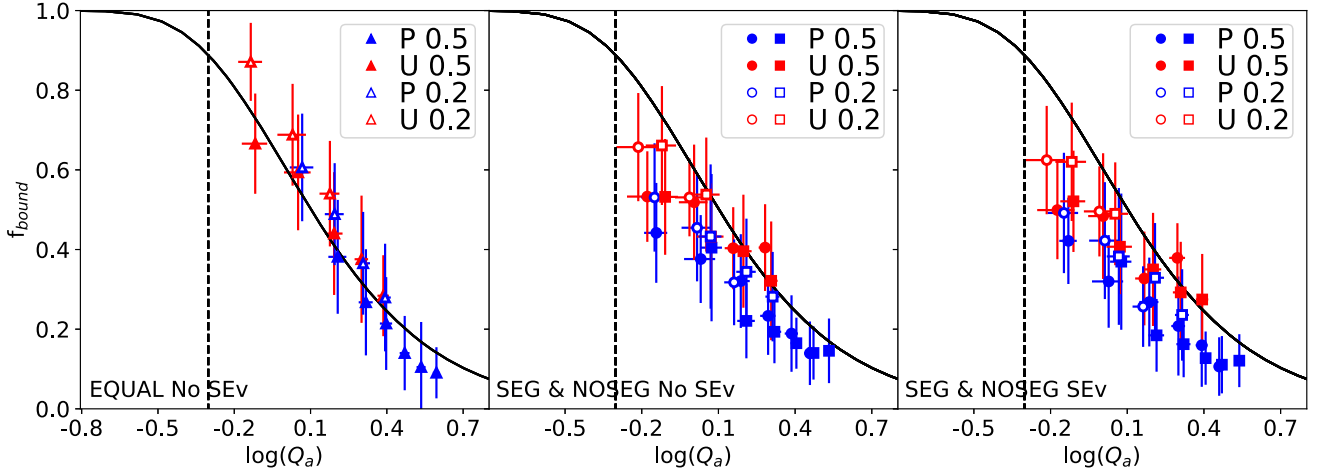


Figure 6. f_{bound} versus $\log(Q_a)$. The order, colour, and symbols are the same as Fig. 4. The solid black line shows the equation (13). Dashed black line is the equilibrium value of $Q = 0.5$ as a reference.

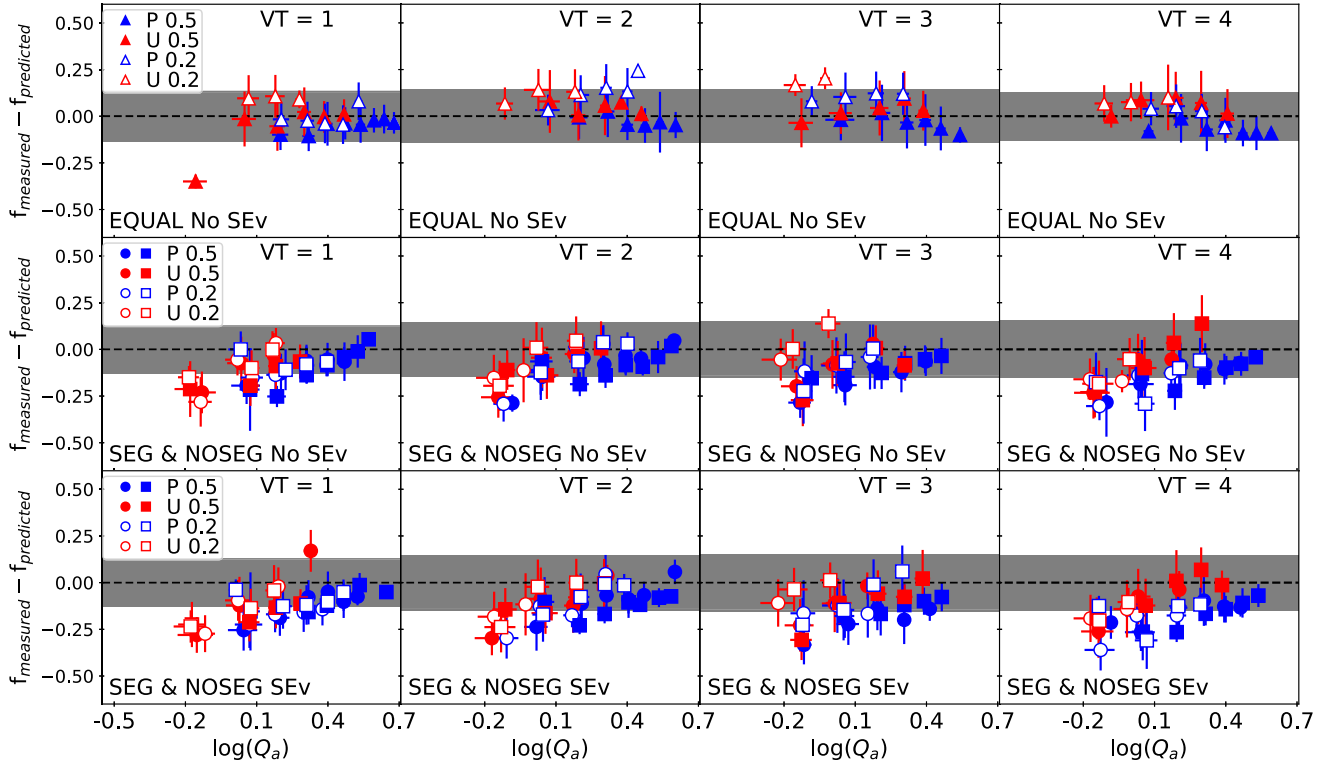


Figure 7. Average difference between the measured bound fraction (f_{measured}) and the predicted bound fraction ($f_{\text{predicted}}$) from equation (13) versus Q_a . The order, colour, and symbols are the same as in Fig. 5.

2.6 Bound mass

We refer as the bound mass f_{bound} to the fraction of stellar mass that is gravitationally bound (M_{bound}) relative to the initial stellar mass M_{init} :

$$f_{\text{bound}} = \frac{M_{\text{bound}}}{M_{\text{init}}}. \quad (11)$$

We measure this value at different times in the evolution of the simulation. We compare the results with the two predictive models

introduced by Farias et al. (2015, 2018). The first model is given by

$$f_{\text{bound}} = \text{erf} \left(\sqrt{\frac{3 \text{LSF}}{2 Q_f}} \right) - \sqrt{\frac{6 \text{LSF}}{\pi Q_f}} \exp \left(-\frac{3 \text{LSF}}{2 Q_f} \right), \quad (12)$$

where LSF is the local stellar fraction introduced by Smith et al. (2011) defined as the SFE measured within the stellar half-mass radius centred on one of the clumps and Q_f is the pre-gas expulsion virial ratio, including the contribution of the BG to the potential felt by the stars. These two quantities are time dependent that contain

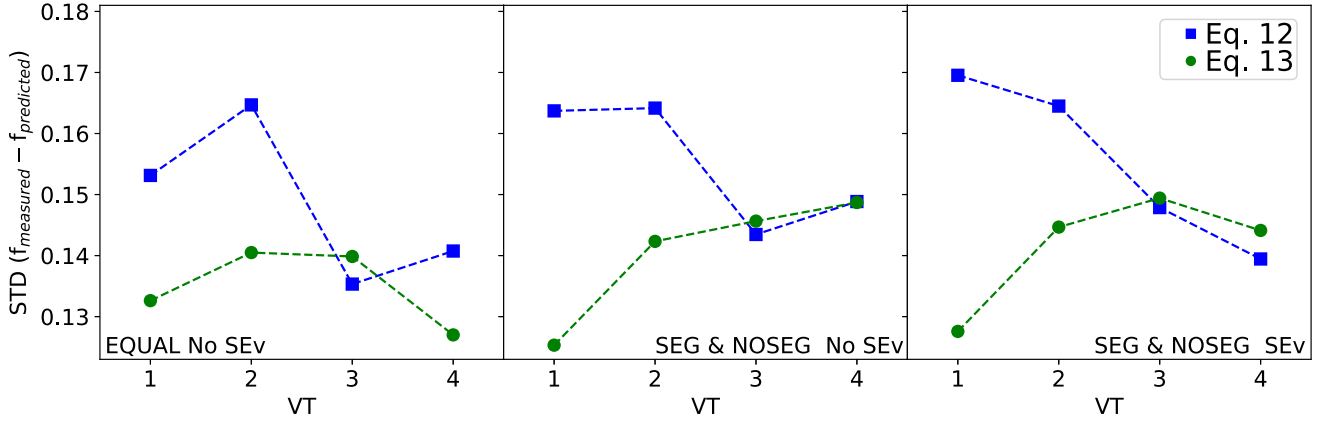


Figure 8. 1σ error value (STD) of the difference between the predicted bound fraction ($f_{\text{predicted}}$) versus virial time. The squares with blue lines are for equation (12) and circles with green line are for equation (13). The panel order is the same as in Fig. 4.

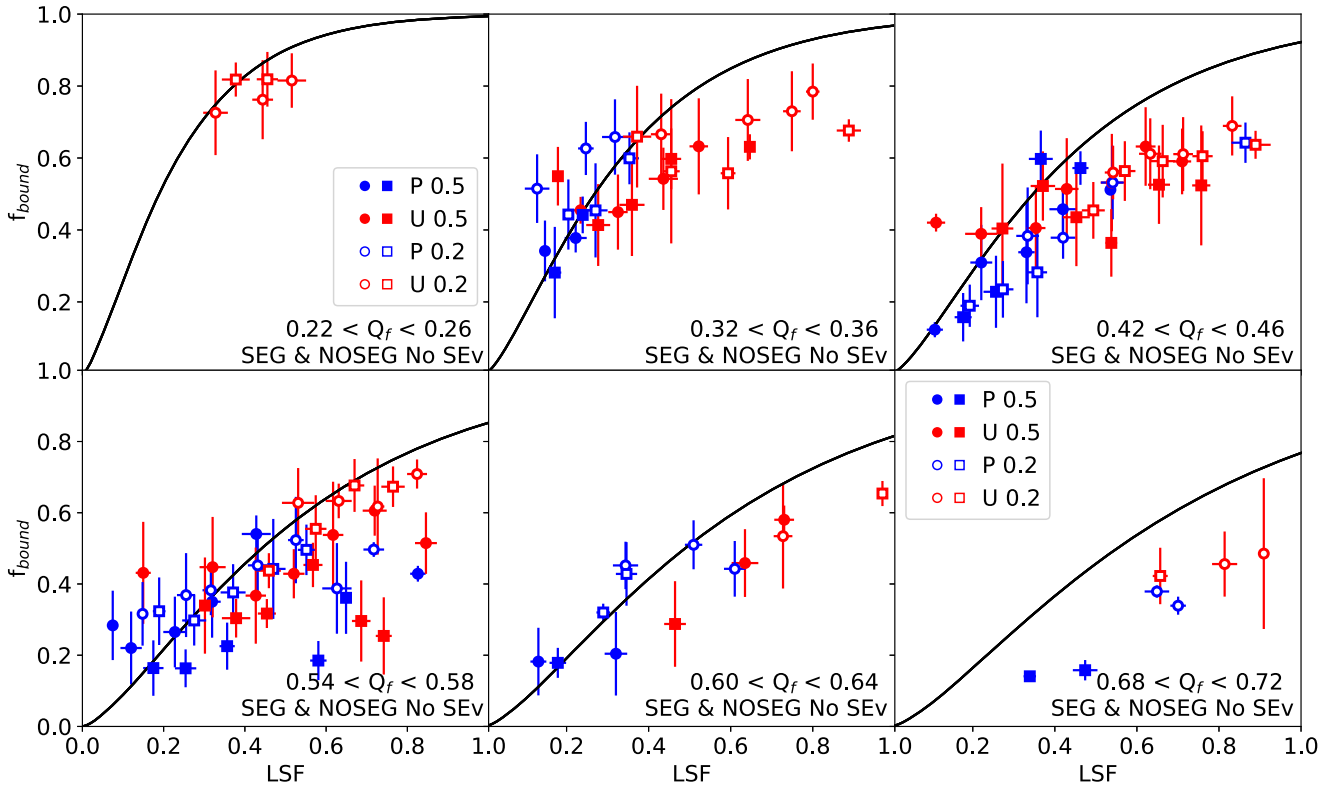


Figure 9. f_{bound} versus LSF for simulations with non-stellar evolution at 16 Myr for VT = 1 (bottom row) and VT = 3 (top row). Colour and symbols are the same as in Fig. 4 where the black line is equation (12).

more information about the stellar distribution at the time when they are measured.

The second model neglects the contribution of the gas to the system. It estimates the amount of bound stellar mass using the virial ratio at the moment of gas expulsion (Q_a), assuming that all gas is expelled instantaneously. The bound stellar fraction is estimated as

$$f_{\text{bound}} = \text{erf}\left(\sqrt{\frac{3}{2}} \frac{1}{Q_a}\right) - \sqrt{\frac{6}{\pi}} \frac{1}{Q_a} \exp\left(-\frac{3}{2} \frac{1}{Q_a}\right). \quad (13)$$

In practice, this model simplifies the estimation of f_{bound} as it only requires information from the stellar component.

These models were successfully tested in a scenario where all stars have the same mass. We also refer to these models as first and second prediction. In this work, we test the reach of these models in a scenario where stars follow a realistic IMF and mass-loss by stellar evolution is included.

3 SET OF SIMULATIONS

For the SEG sample, we create 10 fractal distributions and 10 different IMF samples associated with them. For each pair of positions and masses, we generate 10 different random assignments

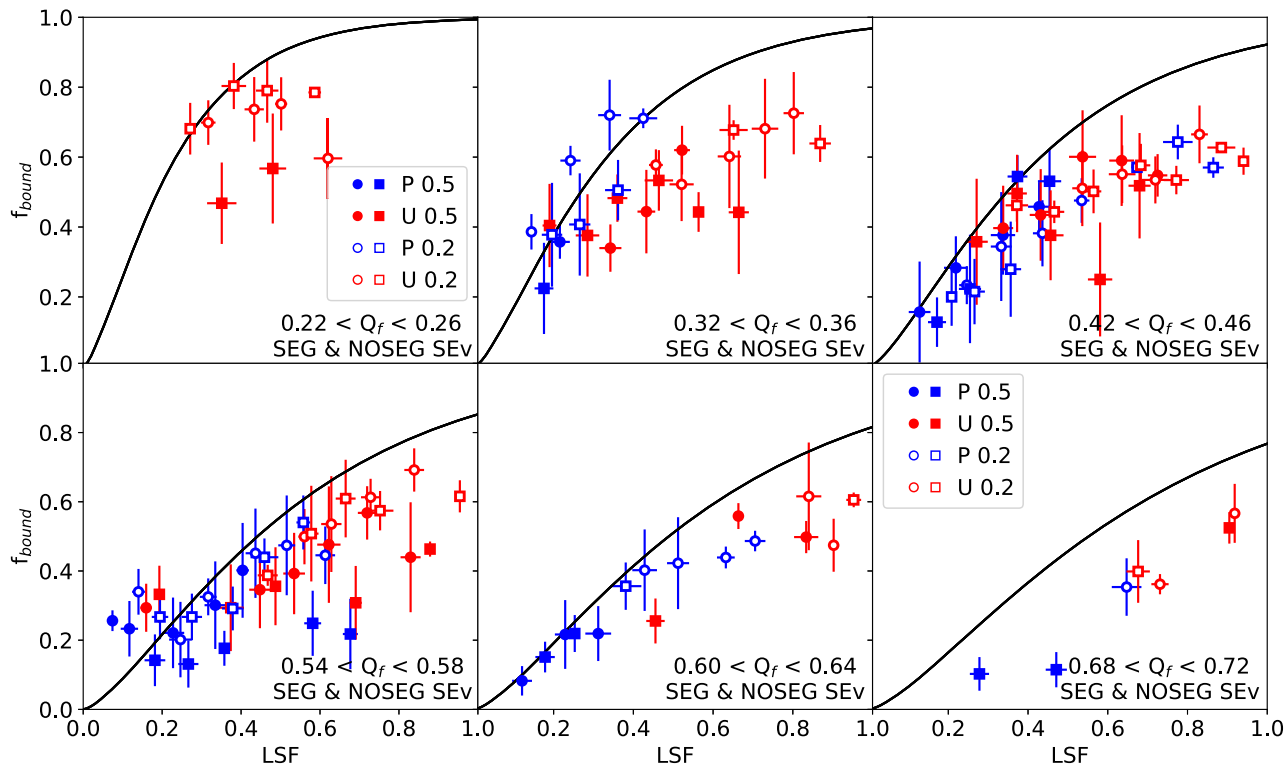


Figure 10. f_{bound} versus LSF for simulations with stellar evolution at 16 Myr for $VT = 1$ (bottom row) and $VT = 3$ (top row). Colours and symbols are the same as in Fig. 4.

of the masses to the positions getting mass segregated clusters, which leads to a total number of 100 simulations. We double the number of simulations scaling the velocities of the particles in order to obtain embedded star clusters starting with $Q_i = 0.5$ and with $Q_i = 0.2$. For each Q_i , the sample is multiplied by four as we have four different VT where we remove the BG finalizing with 800 simulations. We add another sample of 800 simulations as we proceed in the same way to produce the NOSEG sample. We evolve the simulations for 16 Myr using the direct N -body code NBODY6++GPU (Wang et al. 2015) that includes stellar mass-loss from stellar evolution. We double the 1600 SEG and NOSEG simulations running again the same sample, but this time with SEv activated. As we employ the latest version of the code used by Farias et al. (2015, 2018), we also introduce a third sample with other 800 simulations but this time based on equal-mass particles as a control method reproducing the results from our previous works. For the equal-mass particle sample, in order to have the same sample size, we use 100 different fractals and we proceed as before ending up with the same number of simulations. We do not use SEv for equal-mass particle simulations. Altogether, we perform a total number of 4000 simulations. The full sample is summarized in Table 1.

4 RESULTS

As in previous works, we are mostly interested in the fraction of stars that remain bound at a late stage, when any sign of initial structure is already lost, specifically we measure f_{bound} at 16 Myr which corresponds to ~ 14.6 initial crossing times. We reproduce the same plots as already shown in Farias et al. (2015, 2018) for a direct comparison. However, we notice that f_{bound} is not constant after gas expulsion, and therefore we also measure it at early stages

in the evolution, i.e. we determine f_{bound} at the precise moment of gas expulsion (TEXP) and at times $t = 4.8, 6.4, 8, 9.6, 11.2, 12.8,$ and 13.4 Myr. In this way we can see how fast dynamical evaporation is affecting the surviving systems. Note that the exact value of TEXP is different for every cluster, since it is calculated based on their specific virial ratio evolution (see Section 2.4). We use the same times, and $t = 0$ Myr, to observe what value of Δ_{MSR} is achieved relative to the imposed initial conditions.

4.1 Equal-mass simulations

The results of our first 800 simulations sample are used as the control sample and for comparison with the new parameter space introduced in this work.

We reproduce the same plot as shown in Farias et al. (2015) that contains only $VT = 1$ and $VT = 3$. In Fig. 3, we show the resulting bound fractions for this set, measured at 16 Myr for star clusters with different Q_f and BG distributions. Black solid line shows equation (12) using the central value of Q_f described in each panel and the LSF value from x -axis. Blue triangles are simulations under a Plummer BG potential (P) and red triangles are simulations under a Uniform BG potential (U). Filled and empty symbols are representing the initial virial ratios $Q_i = 0.5$ and $Q_i = 0.2$, respectively. The triangles have the average values for f_{bound} at 16 Myr for the simulations with values of LSF and Q_f in the respective range. Note that for the cases where Q_f is sub and supervirial, the exact value of Q is not possible to fix, since each cluster reaches a different peak in Q depending on the initial distribution of stars. Therefore, we cannot fill each panel with the same quantity of points, with the most extreme values of Q_f being the rarest.

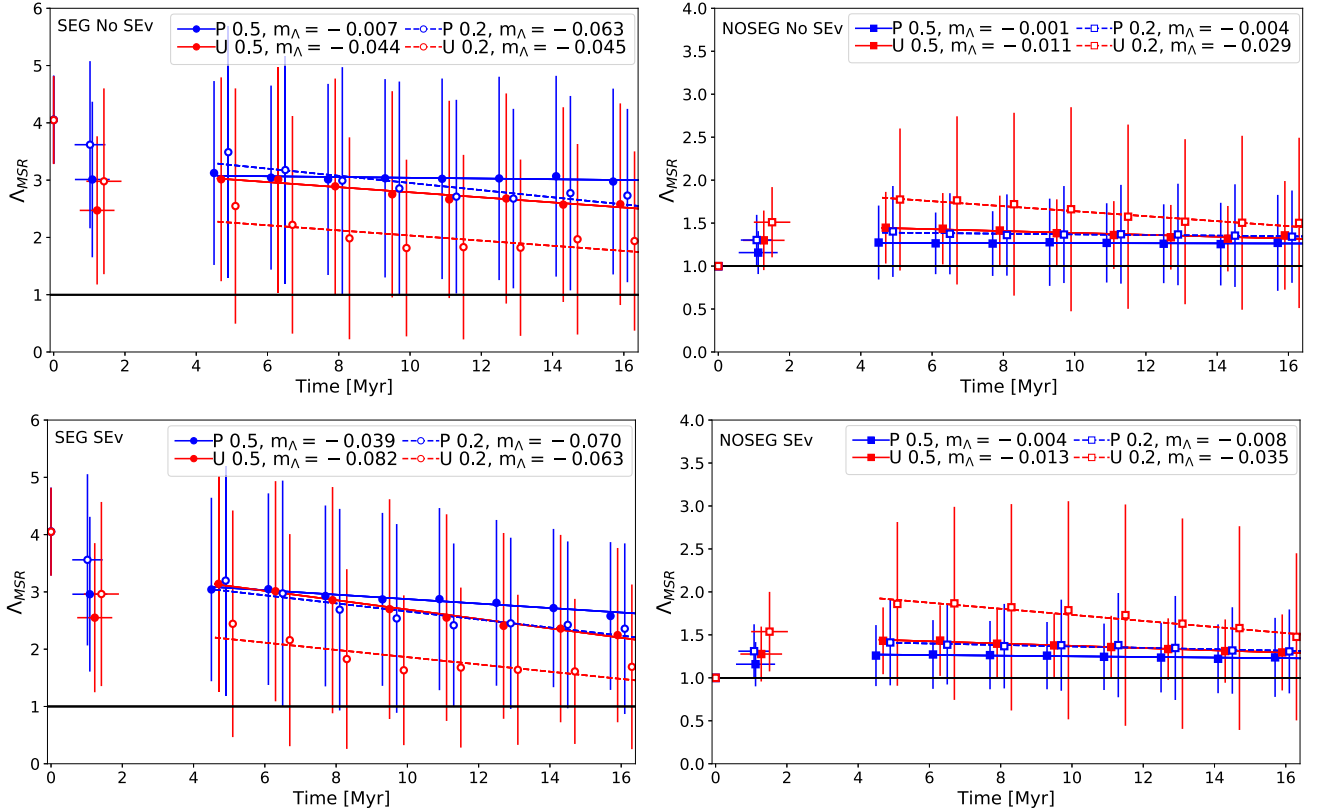


Figure 11. Λ_{MSR} versus time. Colours and symbols are the same as in the previous figures. The solid black line is $\Lambda_{\text{MSR}} = 1$ which means a star cluster not segregated. Simulations in top panels are with No-SEv and bottom panels with SEv. The lines show linear fit according to equation (14) where the slopes m_{Λ} are indicated respectively in the legends.

Table 2. Summary of Λ_{MSR} . First and second columns indicate the BG potential (P = Plummer, U = uniform) with its respective initial virial ratio. The third column refers to the sample initial stellar distribution and if the stellar evolution is on. The fourth column shows the initial Λ_{MSR} value and fifth column is the average time when gas expulsion is done. Sixth column is the Λ_{MSR} at the moment of gas expulsion and last column shows the Λ_{MSR} at 4.8 Myr.

BG	Q_i	Sample/SEv	Initial Λ_{MSR}	Time TEXP	$\Lambda_{\text{MSR, ge}}$	$\Lambda_{\text{MSR, } t=4.8}$
P	0.5	SEG/No	4.05 ± 0.77	1.08 ± 0.49	3.01 ± 1.36	3.12 ± 1.61
P	0.2	SEG/No	4.05 ± 0.76	1.02 ± 0.43	3.62 ± 1.46	3.49 ± 2.19
P	0.5	SEG/Yes	4.06 ± 0.77	1.09 ± 0.49	2.96 ± 1.35	3.04 ± 1.60
P	0.2	SEG/Yes	4.05 ± 0.76	1.02 ± 0.43	3.56 ± 1.49	3.20 ± 2.00
U	0.5	SEG/No	4.05 ± 0.76	1.22 ± 0.49	2.47 ± 1.29	3.01 ± 1.78
U	0.2	SEG/No	4.05 ± 0.77	1.41 ± 0.49	2.98 ± 1.62	2.55 ± 2.05
U	0.5	SEG/Yes	4.05 ± 0.76	1.23 ± 0.49	2.55 ± 1.30	3.14 ± 1.88
U	0.2	SEG/Yes	4.05 ± 0.77	1.41 ± 0.49	2.96 ± 1.61	2.44 ± 1.98
P	0.5	NOSEG/No	1.00 ± 0.02	1.12 ± 0.55	1.16 ± 0.25	1.27 ± 0.43
P	0.2	NOSEG/No	1.00 ± 0.03	1.08 ± 0.45	1.30 ± 0.29	1.40 ± 0.53
P	0.5	NOSEG/Yes	1.00 ± 0.02	1.12 ± 0.55	1.16 ± 0.26	1.26 ± 0.36
P	0.2	NOSEG/Yes	1.00 ± 0.03	1.08 ± 0.44	1.31 ± 0.31	1.41 ± 0.50
U	0.5	NOSEG/No	1.00 ± 0.03	1.28 ± 0.58	1.30 ± 0.35	1.45 ± 0.42
U	0.2	NOSEG/No	1.00 ± 0.02	1.51 ± 0.51	1.51 ± 0.41	1.77 ± 0.83
U	0.5	NOSEG/Yes	1.00 ± 0.02	1.28 ± 0.59	1.28 ± 0.32	1.43 ± 0.39
U	0.2	NOSEG/Yes	1.00 ± 0.02	1.51 ± 0.52	1.54 ± 0.46	1.86 ± 0.95

We observe that the first prediction (equation 12) is more accurate in top panels (star clusters with $Q_i < 0.5$) whereas there is no clear trend in the bottom panels. The reason of this is due to the high levels of substructure still present in the bottom panels. Gas expulsion at

$VT = 1$ is very early and therefore substructure had not had time enough to be erased. The LSF value is sensible to this effect as it needs to find the half-mass star radius centred in one of these subclusters. We also include the results with $VT = 2$ and $VT = 4$

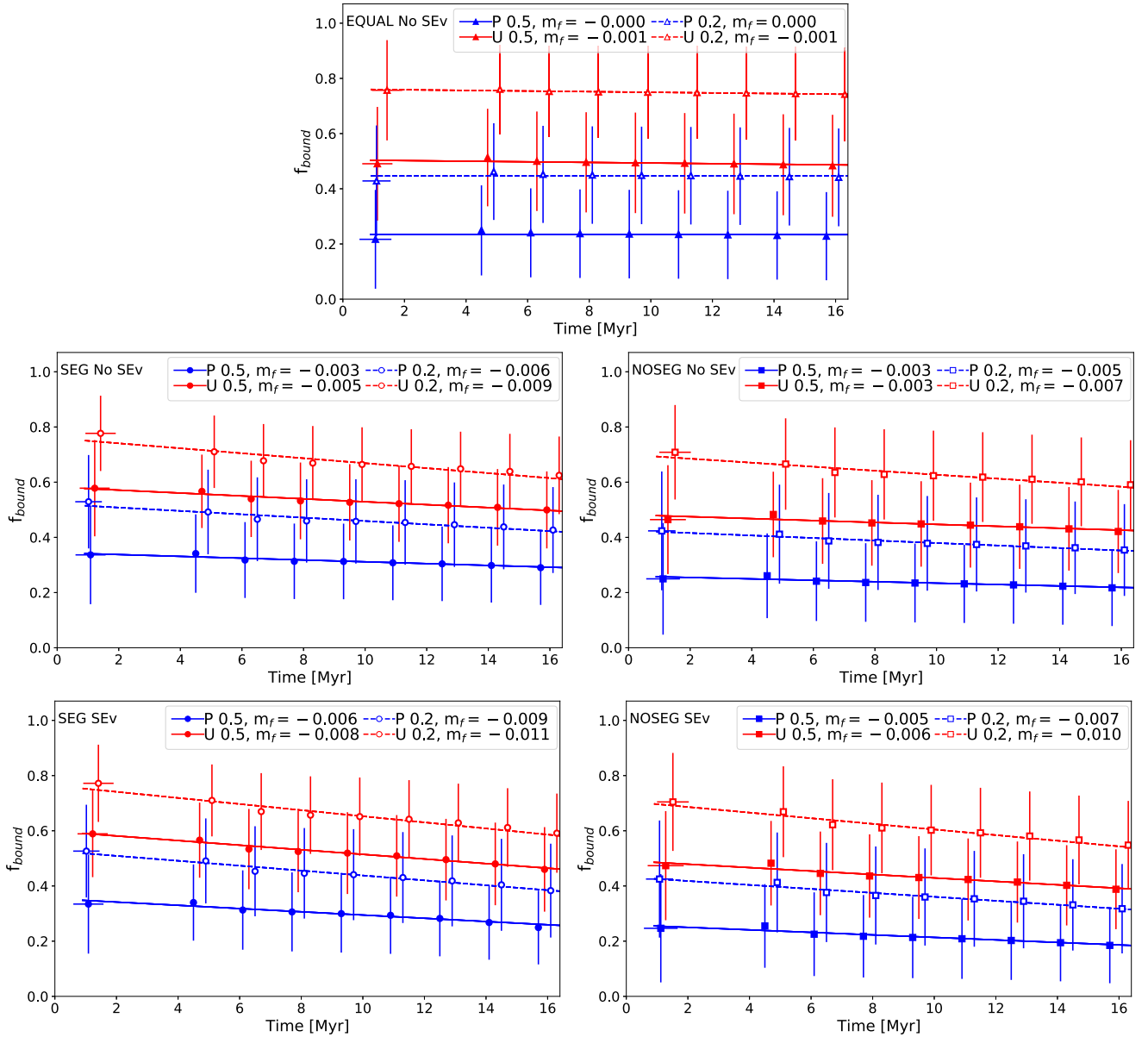


Figure 12. f_{bound} evolution in time. Colours and symbols are the same as in previous figures. The lines show linear fit according to equation (15) where the slopes m_f are indicated respectively in the legends.

in Fig. 4 (left-hand panel). In this case, early and late gas expulsion are mixed and a large dispersion is measured but the prediction still matches the results in 1σ error range. To see the effect of early and later gas expulsion more clearly, we show in Fig. 5, top panels, the average difference between the f_{bound} measured (f_{measured}) and the predicted value from equation (12) ($f_{\text{predicted}}$) divided by VT from left to right. The grey area represents the 1σ error including all the cases, showing less dispersion for VT = 3 and VT = 4. In Fig. 8 (left-hand panel), the blue squares represent the values from the grey zone in Fig. 5 shown independently for a better appreciation. Farias et al. (2015) mostly explored gas expulsion times with VT > 3 when the initial substructure is mostly erased by dynamical processes (Allison et al. 2009b; Parker et al. 2014). The prediction gets much closer to the results at VT \geq 3 and it is expected to get even closer when gas expulsion happens later. Nevertheless, the moment of gas expulsion is kept as shown to make the study more realistic as it has

been constrained that gas expulsion occurs very early for low-mass clusters (Dinnbier & Walch 2020).

In Fig. 6 (left-hand panel), we show the same models, again measured at 16 Myr but as a function of the virial ratio right after gas expulsion, Q_a . Black solid line shows the prediction from equation (13), i.e. using Q_a as single parameter estimator. In this plot, all VT are included. Most of the clusters after gas expulsion become highly supervirial ($Q_a \gg 1$) because of the instant removal of the BG potential. Triangles represent the same initial conditions described before and the values are grouped in bins of $\Delta Q_a = 0.5$. The model corresponding to equation (13) describes the results within the whole Q_a range and it is not sensitive to the VT when the gas expulsion is measured. The latter can be seen in Fig. 7 (top panels), where a similar scatter is present when gas expulsion happens at different VT with only a few exceptions falling outside the grey zone. The dispersion of the results is less for these results as 1σ error is smaller

Table 3. Summary of fitting line slopes for f_{bound} time evolution. First and second columns indicate the BG potential (P = Plummer, U = uniform) with its respective initial virial ratio. The third column refers to the sample initial stellar distribution and if the stellar evolution is on. The fourth column shows the slope of the fitting line measured for each case. Last column shows f_{bound} at the moment of gas expulsion.

BG	Q_i	Sample/SEv	m_f	$f_{\text{bound, ge}}$
P	0.5	EQUAL/No	-0.003	0.23 ± 0.16
P	0.2	EQUAL/No	-0.006	0.44 ± 0.18
U	0.5	EQUAL/No	-0.003	0.48 ± 0.18
U	0.2	EQUAL/No	-0.006	0.74 ± 0.17
P	0.5	SEG/No	-0.003	0.29 ± 0.14
P	0.2	SEG/No	-0.006	0.43 ± 0.16
U	0.5	SEG/No	-0.005	0.50 ± 0.14
U	0.2	SEG/No	-0.009	0.62 ± 0.14
P	0.5	NOSEG/No	-0.003	0.22 ± 0.14
P	0.2	NOSEG/No	-0.005	0.35 ± 0.17
U	0.5	NOSEG/No	-0.003	0.42 ± 0.15
U	0.2	NOSEG/No	-0.007	0.59 ± 0.16
P	0.5	SEG/Yes	-0.006	0.25 ± 0.13
P	0.2	SEG/Yes	-0.009	0.38 ± 0.17
U	0.5	SEG/Yes	-0.008	0.46 ± 0.15
U	0.2	SEG/Yes	-0.011	0.59 ± 0.14
P	0.5	NOSEG/Yes	-0.005	0.18 ± 0.14
P	0.2	NOSEG/Yes	-0.007	0.32 ± 0.16
U	0.5	NOSEG/Yes	-0.006	0.39 ± 0.14
U	0.2	NOSEG/Yes	-0.010	0.55 ± 0.16

than before. Fig. 8 (left-hand panel) shows the width of the grey area for this prediction, with the green circles being smaller for three of the four VT. Therefore, the description provided by equation (13) is more suitable for our work since most of our simulations in this work expel the gas at very early times when high levels of substructure are still present.

4.2 SEG-NOSEG simulations with no SEv

The results for SEG and NOSEG simulations with No-SEv at 16 Myr for VT = 1 and VT = 3 are shown in Fig. 9. The symbols are the same as before. For these cases, circles indicate simulations starting with SEG and squares for simulations starting with NOSEG.

We observe that in most cases equation (12) overestimates f_{bound} , especially at higher values of LSF. We also include the results when $Q_f = 0.5$ (VT = 2 and VT = 4) in Fig. 4 (central panel), where we observe the same behaviour.

We test equation (13) in Fig. 6 with the same symbols as before, where all VT are included. Again, at 16 Myr, most of the simulations have lower values of f_{bound} than expected. SEG and NOSEG simulations show the same behaviour, with both analytical models overestimating the bound fraction. When using equation (12) many dots are outside the 1σ error bars, while equation (13) does a better job with estimations mostly within error bars.

The question of how early and late gas expulsion influence the accuracy of the prediction is addressed in Figs 5 and 7 (second row) for the first prediction and second prediction, respectively. For equation (12), we observe that independent of the VT, the results are mostly out of the grey zone especially for higher LSF. For equation (13), more results are falling inside 1σ error zone with

exceptions for low Q_a . This behaviour is better appreciable in Fig. 8, where the dispersion for the results of the first prediction (blue squares) compared to the second prediction (green circles) is larger for VT ≤ 2 and in the same range for VT ≥ 3 . Besides the *individual results*, in most of the cases, f_{bound} is found below the predictions.

4.3 SEG-NOSEG simulations with SEv

The results for SEG and NOSEG simulations with SEv at 16 Myr for VT = 1 and VT = 3 are shown in Fig. 10. The symbols are the same as before. The values of LSFs are not expected to be identical for all pairs of simulations started with SEv and No-SEv due to small changes in the orbit calculations done in a N -body simulation. We observe as before that the prediction equation (12) overestimates f_{bound} . The number of simulations far from the curve is higher for this sample and the same is observed for $Q_f = 0.5$ (VT = 2,4) in Fig. 4 (right-hand panel).

The prediction from equation (13) is shown in Fig. 6 with the same symbols as before. The values of f_{bound} at the end of most simulations are even smaller than when we do not use SEv.

As in the previous cases, we test early and late gas expulsion in Figs 5 and 7 (bottom panels). The same description previously mentioned for the simulations without SEv is applicable for these results but now with a larger number of simulations outside of the grey area. In Fig. 8, we observe a small improvement in the dispersion of the results when VT = 4, if we compare with its pair in the central panel.

4.4 Mass segregation

We show in Fig. 11 the time evolution of Λ_{MSR} . The symbols are the same as before and the solid black line is $\Lambda_{\text{MSR}} = 1$ which means a stellar distribution where massive stars are distributed the same way as low-mass stars, i.e. without mass segregation.

The left top panel is the evolution of mass segregation for simulations starting with SEG initial stellar distribution, and No-SEv. At the beginning, $\Lambda_{\text{MSR}} = 4.05 \pm 0.77$ for all cases as they are the same fractals with the same IMF samples. At the moment of gas expulsion, which happens typically at a time of 1.18 ± 0.50 Myr, the level of mass segregation decreases until it reaches $\Lambda_{\text{MSR}} = 3.02 \pm 1.49$. On the other hand, the simulations in the right-hand panel at $t = 0$ Myr have $\Lambda_{\text{MSR}} = 1.00 \pm 0.02$. At the moment of gas expulsion at $t = 1.25 \pm 0.55$ Myr, the level of mass segregation increases to an average value of $\Lambda_{\text{MSR}} = 1.32 \pm 0.35$. The same behaviour is observed in the bottom panels, where stellar evolution is activated. Initial values are the same as they are from the same clusters. Small differences can appear due to the randomness of choosing the sample of low-mass stars for the calculation of Λ_{MSR} (see Section 2.2). The evolution of the virial ratio is very similar since only SEv mass-loss from winds acts on time-scales $\lesssim 1$ Myr for most of the stars. In the left-hand panel at $t = 1.19 \pm 0.50$, the mass segregation on average is $\Lambda_{\text{MSR}} = 3.01 \pm 1.48$ and in right-hand panel at $t = 1.25 \pm 0.55$ it is $\Lambda_{\text{MSR}} = 1.32 \pm 0.37$. The values for each of the cases are summarized in Table 2. The gas expulsion for simulations with uniform BG potential is slightly later than simulations with Plummer BG potential.

As reported in Domínguez et al. (2017) and Pavlík, Kroupa & Šubr (2019), we see that clusters with initial mass segregation rapidly decrease their levels during the embedded phase, as they relax into a more stable configuration. On the other hand, clusters with NOSEG initial stellar distribution start raising their mass segregation levels until gas expulsion happens.

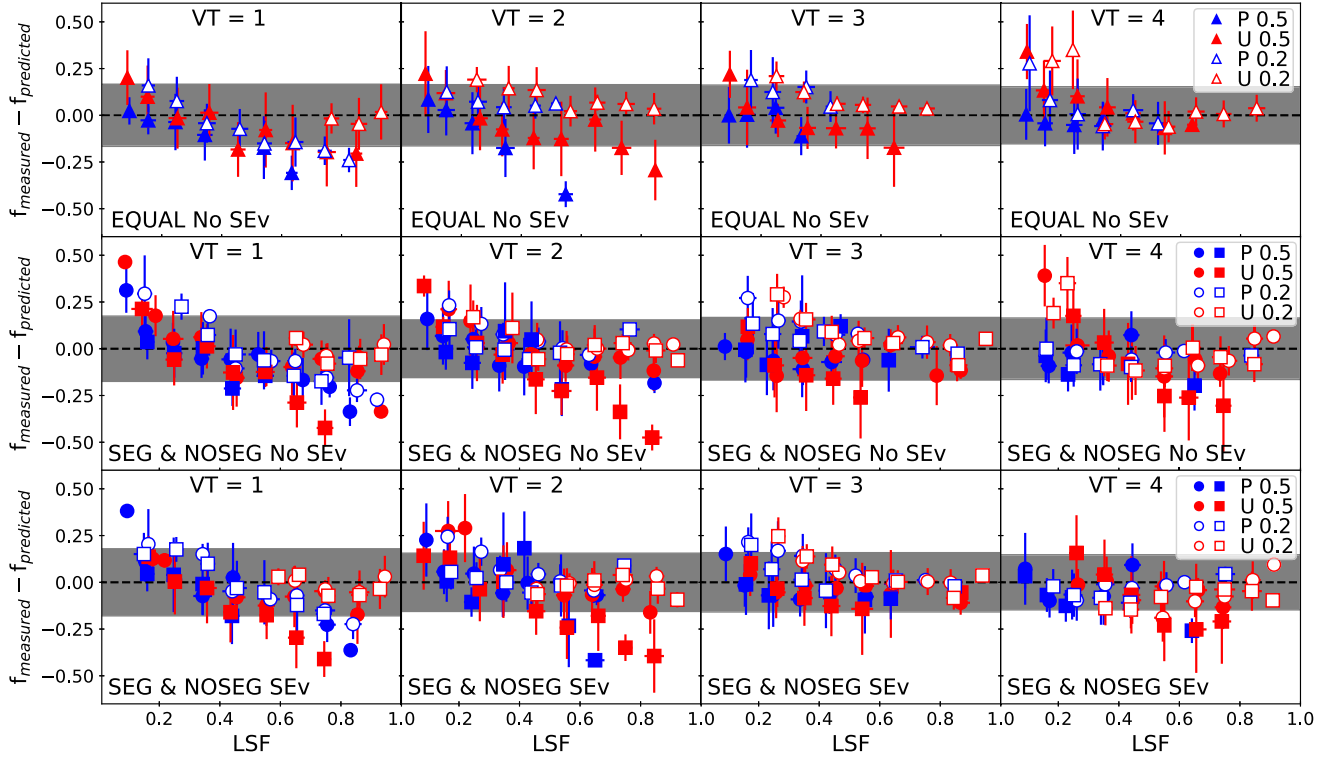


Figure 13. Same as Fig. 5 but for the moment of the gas expansion.

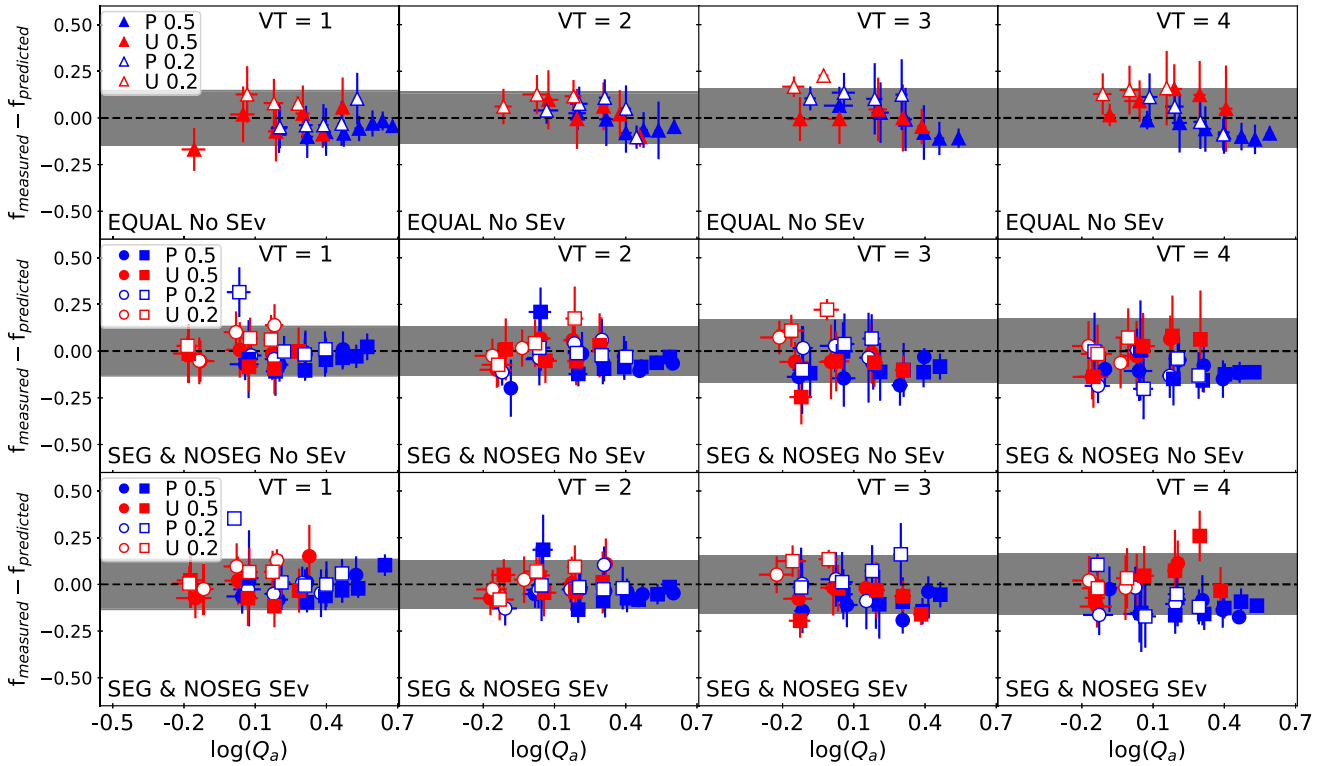


Figure 14. Same as Fig. 7 but now for the moment of the gas expansion.

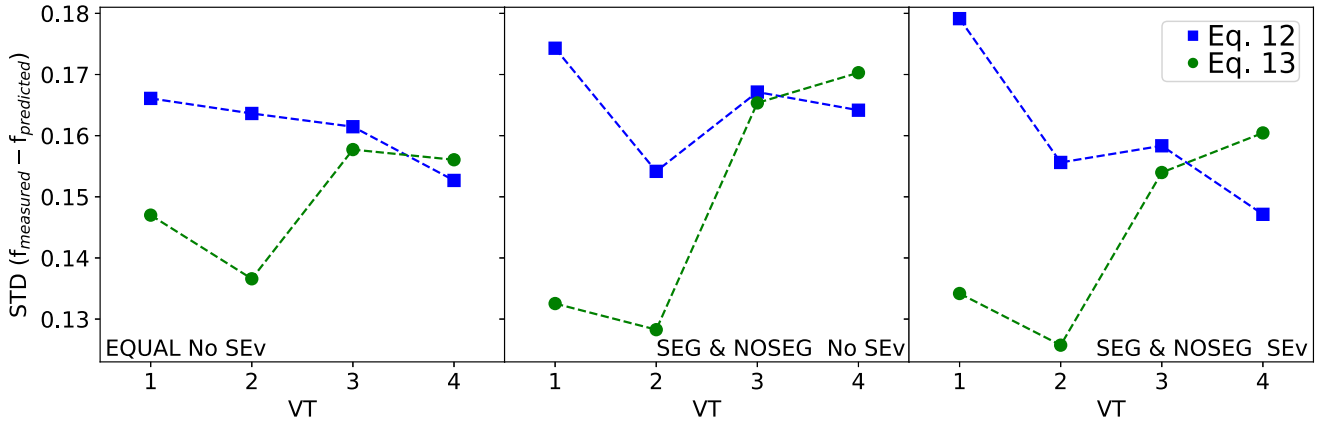


Figure 15. Same as in Fig. 8, but now f_{bound} is measured at the moment of the gas expulsion.

We include a linear fit for times ≥ 4.8 Myr to each pair of initial conditions with the form:

$$\Lambda_{\text{MSR}}(t) = m_{\Lambda}t + \Lambda_{\text{MSR}, t=4.8}, \quad t \geq 4.8, \quad (14)$$

where m_{Λ} is the slope of the fit in units of Myr^{-1} and $\Lambda_{\text{MSR}, t=4.8}$ is the Λ_{MSR} at 4.8 Myr, which is shown in Table 2, last column. As the clusters expand after gas expulsion, the value of Λ_{MSR} shows a continuous decrease ($m_{\Lambda} < 0$), being steeper for SEG simulations. Simulations with SEv are shown in the bottom panels. In this case, the decrease of Λ_{MSR} is steeper as the more massive stars explode as SNe.

4.5 Dynamical evaporation

As we have introduced different masses, stronger interactions between the stars are expected, leading to the ejection of stars. In addition, SEv adds another source of mass-loss. In Fig. 12, we show the f_{bound} evolution using the same symbols as in the previous figures. We include a linear fit to each pair of initial conditions with the form:

$$f(t) = m_f t + f_{\text{bound,ge}}, \quad t \geq \text{TEXP}, \quad (15)$$

where m_f is the slope of the fit in units of Myr^{-1} and $f_{\text{bound,ge}}$ is the bound fraction at the moment of gas expulsion. A summary table of both parameters is shown in Table 3. While all measurements are taken at the same times, i.e. at $t = 4.8, 6.4, 8, 9.6, 11.2, 12.8, 13.4,$ and 16 Myr, they are slightly shifted for clarity.

In the top panel, the time evolution of f_{bound} is shown for simulations with equal-mass particles (triangles). For the four cases are observed practically constants f_{bound} values, as we measure two slopes with $m_f = -0.001$ for Plummer BG (P) and two slopes with $m_f = 0$ for uniform BG (U).

In the panels where simulations with No-SEv are shown, we observe in both cases negative slopes with values $-0.003 \leq m_f \leq -0.009$ independent of the initial conditions. SEG simulations under uniform BG potential with $Q_i = 0.2$ show the steepest slope.

In the bottom panels, where simulations with SEv are shown, we observe even steeper slopes with values $-0.005 \leq m_f \leq -0.011$ also independent of the initial conditions. As in the central panels, we measure the steepest slope in the left-hand panel under the same initial conditions.

The highest values of f_{bound} are shown in all cases at the moment of gas expulsion, and continuously decrease thereafter (SEG-NOSEG). In Figs 13 and 14, we show again the average difference with the

prediction but now compared with the value of f_{bound} measured at the moment of gas expulsion. At this moment, both equations (12) and (13) can closely describe our results, with the first prediction, compared with equal-mass results, still showing larger dispersion for early VT, but in the same range for later gas expulsion and, this is independent of the inclusion or not of SEv. The dispersion observed for the different cases at the moment of the gas expulsion are shown in Figs 15 and 7. We summarize in Table 3 the different fitting line slopes together with their respective f_{bound} at the moment of gas expulsion. We find that independent of the intrinsic characteristics in our sample, they show decreasing slopes, as stars are ejected. On a first order, models with a Plummer background potential have stronger slopes than uniform background potential. And to second order, star clusters with $Q_i = 0.5$ have steeper slopes than initially cold star clusters.

5 SUMMARY AND CONCLUSION

In this work, we test two models introduced by Farias et al. (2015, 2018) that predict the fraction of bound mass that star clusters can retain after explosive gas expulsion. These models were previously tested only using equal-mass particle and fractal star clusters. Here, we explore how these models work on a more realistic scenario, introducing an IMF with two different particle distribution for the primordial location of massive stars. We first assume massive stars are born in random locations within the star cluster (NOSEG), and models with high levels of primordial mass segregation (SEG). In both cases, we also investigate the effects of SEv. We create a sample of 800 simulations to minimize stochastic fluctuations for every set and combination of the new parameters.

Since we use the latest version of the NBODY6++ code, we start by reproducing the previous results with equal-mass particles. In order to be consistent with recent evidence of a very early release of gas in low-mass clusters ~ 1 Myr (Dinnbier & Walch 2020), we set the moment of gas expulsion at an early time.

The first predictive model, which depends on the LSF and the pre-gas expulsion virial ratio, we find that the results are more accurate when star clusters expel their gas at later stages, i.e. when the level of substructure is reduced by dynamical processes, in agreement with our previous works. The second predictive model that only depends of one parameter, the post-gas expulsion virial ratio, is not sensible to substructure, confirming previous results tested with

highly substructured BG models, and indicating that the nature of the BG makes no difference for this specific model.

We introduce random IMF samples with different levels of primordial mass segregation as quantified by Λ_{MSR} and contrast with previous work. Star clusters with no primordial mass segregation show a lower concentration of massive stars at the moment of gas expulsion compared to clusters with primordial segregation. Non-segregated star clusters are still raising their concentration of stars when gas is removed, as reported in previous work using similar frameworks (see e.g. Allison et al. 2010; Yu et al. 2011; Domínguez et al. 2017). We find an average $\Lambda_{\text{MSR}} \sim 1.32$ implying that all clusters in this work are mass segregated at the moment of gas expulsion, regardless of the initial conditions.

After gas expulsion, Λ_{MSR} is observed for a short time to be even higher, followed by a continuous decrease due to cluster expansion. For the case of simulations with SEv, the SNe occurring in the second half of the simulation results in a steeper decrease.

By introducing random IMF samples, f_{bound} measurements at 16 Myr are in most of the cases below the predicted curves and with larger deviations when SEv is included. By examining the evolution in time of f_{bound} , we observe a continuous decrease or a negative slope, also known as dynamical evaporation. The average values of f_{bound} are much closer to the predictions when they are measured at the moment of gas expulsion. For equal-mass particles, the evaporation slopes are close to be zero, i.e. the predictions from the model are matched independent of the time we measure f_{bound} as it stays practically constant.

For simulations with SEv, at the moment of gas expulsion, we observe a similar trend. While SEv mass-loss should decrease the bound mass, our simulations show that this is not the case at early times. Our low-mass clusters contain only a few very massive stars ($M > 20 M_{\odot}$) and only stellar winds change the mass at an early phase. These few massive stars evolve as SNe in the second part of the simulation and thus we only observe differences at later times.

We conclude that independent of the initial conditions, the predictive analytical models introduced by Farias et al. (2015, 2018) can describe our results when measuring close to the gas expulsion time, but they overestimate f_{bound} at later stages. Dynamical evaporation due to two-body interactions is stronger in stellar systems having different stellar masses and it is the main reason for the continuous decrease of f_{bound} . The inclusion of SEv can only decrease f_{bound} at later stages due to SNe mass-loss. Moreover, no significant differences are observed at early times when only stellar winds take action. Initial mass distribution (SEG or NOSEG) does not play a role in our results. This is due to the fact that all clusters studied have rapidly become dynamically mass segregated, irrespective of the details of the initial conditions. We emphasize that the gas expulsion scheme studied here is the most destructive scenario and any smoothing applied to the process would improve the chances to find larger f_{bound} .

Whether or not our initial conditions are a realistic state of an embedded star cluster is a matter of discussion. It has been shown that the pre-gas expulsion of a young massive star cluster ($M > 10^4 M_{\odot}$) is very compact (Marks & Kroupa 2012) and the number of substructures weakly depend on their total mass. An example of this is R136 in the 30 Doradus nebula with a total mass $> 2.2 \times 10^4 M_{\odot}$ with a radius poorly constrains to be ~ 2 pc. Authors (see e.g. Silich & Tenorio-Tagle 2017) also suggest that this object is not result of a single starburst and probably a (re)-collapse of gas which already gave birth to an older generation of stars where both together are part of NGC 2070, and this scenario differs with the one developed here. In this work, the low-mass embedded star clusters ($M = 2.5 \times 10^3$

M_{\odot}) show substructures at the moment of gas expulsion and these are decreasing as we wait to remove the gas. The aim of this work is to study if this non-spherical distribution helps the cluster to deal better with the violent gravitational potential change and to survive with $\text{SFE} = 0.20$ otherwise if we wait until the substructures are erased we would reproduce the same scenario largely studied in Baumgardt & Kroupa (2007) with non-surviving clusters in this range of SFE.

ACKNOWLEDGEMENTS

We acknowledge support from CONICYT (CONICYT-PFCHA/Doctorado acuerdo bilateral DAAD/62170008), financial support from DAAD (funding program number 57395809). The authors acknowledge support by the state of Baden-Württemberg through bwHPC and the German Research Foundation (DFG) through grant INST 35/1134-1 FUGG and Heidelberg cluster of excellence EXC 2181 (Project-ID 390900948) ‘STRUCTURES: A unifying approach to emergent phenomena in the physical world, mathematics, and complex data’ funded by the German Excellence Strategy. JPF acknowledges support from ERC Advanced Grant MSTAR. MF acknowledges funding from FONDECYT regular N° 1180291, BASAL N° AFB-170002 (CATA). RSK acknowledges financial support from the DFG via the collaborative research center SFB 881 ‘The Milky Way System’ (project ID 138713538, subprojects B1, B2, B8).

DATA AVAILABILITY STATEMENT

The data of the full set of simulations (see Table 1) presented in this article will be shared on reasonable request to the corresponding author.

REFERENCES

- Adams F. C., 2000, *ApJ*, 542, 964
Allison R. J., Goodwin S. P., Parker R. J., Portegies Zwart S. F., de Grijs R., Kouwenhoven M. B. N., 2009a, *MNRAS*, 395, 1449
Allison R. J., Goodwin S. P., Parker R. J., de Grijs R., Portegies Zwart S. F., Kouwenhoven M. B. N., 2009b, *ApJ*, 700, L99
Allison R. J., Goodwin S. P., Parker R. J., Portegies Zwart S. F., de Grijs R., 2010, *MNRAS*, 407, 1098
Banerjee S., Kroupa P., 2018, in Stahler S., ed., *The Birth of Star Clusters*, Vol. 424. Springer, Cham, p. 143
Bastian N., Goodwin S. P., 2006, *MNRAS*, 369, L9
Baumgardt H., Kroupa P., 2007, *MNRAS*, 380, 1589
Boily C. M., Kroupa P., 2003a, *MNRAS*, 338, 665
Boily C. M., Kroupa P., 2003b, *MNRAS*, 338, 673
Bonatto C., Bica E., 2006, *A&A*, 455, 931
Bonnell I. A., Bate M. R., 2006, *MNRAS*, 370, 488
Bonnell I. A., Davies M. B., 1998, *MNRAS*, 295, 691
Bonnell I. A., Bate M. R., Clarke C. J., Pringle J. E., 1997, *MNRAS*, 285, 201
Bonnell I. A., Bate M. R., Clarke C. J., Pringle J. E., 2001, *MNRAS*, 323, 785
Brinkmann N., Banerjee S., Motwani B., Kroupa P., 2017, *A&A*, 600, A49
Chen L., de Grijs R., Zhao J. L., 2007, *AJ*, 134, 1368
di Francesco J. et al., 2010, *A&A*, 518, L91
Dib S., Henning T., 2019, *A&A*, 629, A135
Dinnbier F., Walch S., 2020, *MNRAS*, 499, 748
Domínguez R., Fellhauer M., Blańa M., Farias J. P., Dabringhausen J., 2017, *MNRAS*, 472, 465
Elmegreen B. G., Krakowski A., 2001, *ApJ*, 562, 433
Er X.-Y., Jiang Z.-B., Fu Y.-N., 2013, *Res. Astron. Astrophys.*, 13, 277

- Farias J. P., Smith R., Fellhauer M., Goodwin S., Candlish G. N., Blaña M., Domínguez R., 2015, *MNRAS*, 450, 2451
- Farias J. P., Tan J. C., Chatterjee S., 2017, *ApJ*, 838, 116
- Farias J. P., Fellhauer M., Smith R., Domínguez R., Dabringhausen J., 2018, *MNRAS*, 476, 5341
- Fellhauer M., Kroupa P., 2005, *ApJ*, 630, 879
- Geyer M. P., Burkert A., 2001, *MNRAS*, 323, 988
- Girichidis P., Federrath C., Allison R., Banerjee R., Klessen R. S., 2012, *MNRAS*, 420, 3264
- Goodwin S. P., 1997, *MNRAS*, 284, 785
- Goodwin S. P., Whitworth A. P., 2004, *A&A*, 413, 929
- Gutermuth R. A., Megeath S. T., Myers P. C., Allen L. E., Pipher J. L., Fazio G. G., 2009, *ApJS*, 184, 18
- Hillenbrand L. A., 1997, *AJ*, 113, 1733
- Hillenbrand L. A., Hartmann L. W., 1998, *ApJ*, 492, 540
- Hills J. G., 1980, *ApJ*, 235, 986
- Johnstone D., Wilson C. D., Moriarty-Schieven G., Joncas G., Smith G., Gregersen E., Fich M., 2000, *ApJ*, 545, 327
- Kirk H., Johnstone D., Tafalla M., 2007, *ApJ*, 668, 1042
- Klessen R., 2001, in Montmerle T., André P., eds, ASP Conf. Ser. Vol. 243, From Darkness to Light: Origin and Evolution of Young Stellar Clusters. Astron. Soc. Pac., San Francisco, p. 139
- Könyves V. et al., 2010, *A&A*, 518, L106
- Kroupa P., 2002, *Science*, 295, 82
- Lada C. J., Alves J., Lada E. A., 1996, *AJ*, 111, 1964
- Larson R. B., 1982, *MNRAS*, 200, 159
- Lee P. L., Goodwin S. P., 2016, *MNRAS*, 460, 2997
- McMillan S. L. W., Vesperini E., Portegies Zwart S. F., 2007, *ApJ*, 655, L45
- Lada C., Margulis M., Dearborn D., 1984, *ApJ*, 285, 141
- Marks M., Kroupa P., 2012, *A&A*, 543, A8
- Maury A. J., André P., Men'shchikov A., Könyves V., Bontemps S., 2011, *A&A*, 535, A77
- Megeath S. T. et al., 2016, *AJ*, 151, 5
- Murray N., 2011, *ApJ*, 729, 133
- Murray S. D., Lin D. N. C., 1996, *ApJ*, 467, 728
- Parker R. J., Goodwin S. P., 2015, *MNRAS*, 449, 3381
- Parker R. J., Wright N. J., Goodwin S. P., Meyer M. R., 2014, *MNRAS*, 438, 620
- Parker R. J., Goodwin S. P., Wright N. J., Meyer M. R., Quanz S. P., 2016, *MNRAS*, 459, L119
- Pavlík V., Kroupa P., Šubr L., 2019, *A&A*, 626, A79
- Plummer H. C., 1911, *MNRAS*, 71, 460
- Raboud D., Mermilliod J. C., 1998, *A&A*, 333, 897
- Schmeja S., Kumar M. S. N., Ferreira B., 2008, *MNRAS*, 389, 1209
- Shukirgaliyev B., Parmentier G., Berczik P., Just A., 2017, *A&A*, 605, A119
- Shukirgaliyev B., Parmentier G., Just A., Berczik P., 2018, *ApJ*, 863, 171
- Shukirgaliyev B., Parmentier G., Berczik P., Just A., 2020, in Bragaglia A., Davies M., Sills A., Vesperini E., eds, Proc. IAU Symp. 351, Star Clusters: From the Milky Way to the Early Universe. Kluwer, Dordrecht, p. 507
- Silich S., Tenorio-Tagle G., 2017, *MNRAS*, 465, 1375
- Smith R., Fellhauer M., Goodwin S., Assmann P., 2011, *MNRAS*, 414, 3036
- Tutukov A. V., 1978, *A&A*, 70, 57
- Wang P., Li Z.-Y., Abel T., Nakamura F., 2010, *ApJ*, 709, 27
- Wang L., Spurzem R., Aarseth S., Nitadori K., Berczik P., Kouwenhoven M. B. N., Naab T., 2015, *MNRAS*, 450, 4070
- Whitmore B. C., Zhang Q., Leitherer C., Fall S. M., Schweizer F., Miller B. W., 1999, *AJ*, 118, 1551
- Wright N. J., Parker R. J., Goodwin S. P., Drake J. J., 2014, *MNRAS*, 438, 639
- Yu J., de Grijs R., Chen L., 2011, *ApJ*, 732, 16
- Zinnecker H., 1982, *Ann. New York Acad. Sci.*, 395, 226

This paper has been typeset from a $\text{\TeX}/\text{\LaTeX}$ file prepared by the author.